Science Arts & Métiers (SAM)
is an open access repository that collects the work of Arts et Métiers Institute of Technology researchers and makes it freely available over the web where possible.

This is an author-deposited version published in: https://sam.ensam.eu
Handle ID: .http://hdl.handle.net/10985/22155

To cite this version :

M. AYAD, L. LAPOSTOLLE, A. RONDEPIERRE, C. LE BRAS, M. SCIUS-BERTRAND, S. ÜNALDI, U. TRDAN, Y. ROUCHAUSSE, J. GRASSY, T. MAILLOT, V. LAPOUJADE, C. MICHEL, L. BERTHE - Modeling of multi-edge effects in the case of laser shock loadings applied on thin foils: Application for material characterization of aluminum alloys - Journal of Applied Physics - Vol. 131, n°9, p.095902 - 2022

Any correspondence concerning this service should be sent to the repository Administrator : scienceouverte@ensam.eu

Modeling of multi-edge effects in the case of laser shock loadings applied on thin foils: Application for material characterization of aluminum alloys

Cite as: J. Appl. Phys. **131**, 095902 (2022); doi: 10.1063/5.0080326
Submitted: 30 November 2021 · Accepted: 5 February 2022 ·
Published Online: 3 March 2022

M. Ayad,[1,a)] L. Lapostolle,[1] A. Rondepierre,[1,2] C. Le Bras,[1,3] M. Scius-Bertrand,[1,4] S. Ünaldi,[1] U. Trdan,[5] Y. Rouchausse,[1] J. Grassy,[6] T. Maillot,[6] V. Lapoujade,[6] C. Michel,[6] and L. Berthe[1,b)]

AFFILIATIONS

[1]PIMM, UMR8006 ENSAM, CNRS, CNAM, 151 bd de l'Hôpital, 75013 Paris, France
[2]THALES LAS France, 78990 Elancourt, France
[3]Airbus Operation S.A.S, 316 route de Bayonne-B.P.D4101, CEDEX 9, F-31060 Toulouse, France
[4]CEA, DAM, DIF, 91297 Arpajon, France
[5]Faculty of Mechanical Engineering, University of Ljubljana, Aškerčeva cesta 6, 1000 Ljubljana, Slovenia
[6]DYNAS+, 5, Avenue Didier Daurat, 31400 Toulouse, France

Note: This paper is part of the Special Topic on Shock Behavior of Materials.
[a)]**Author to whom correspondence should be addressed:** mohammad.ayad@ensam.eu
[b)]**Electronic mail:** laurent.berthe@cnrs.fr

ABSTRACT

This article presents the study of the shock wave propagation through aluminum alloys (pure aluminum and aluminum 2024-T3) produced by laser plasma using experimental and numerical tests. Water confinement regime interaction, pulse duration (7.2 ns), and power density (1–5 GW/cm^2) range correspond to laser shock peening process configuration and parameters. To that scope, we simulate the shock wave propagation using non-linear explicit code LS-DYNA, which we validate with experimental results. Thereupon, we present a descriptive analysis that links separately the material model and loading conditions to the dynamic response of aluminum alloys under high strain rate laser shock by coupling the Johnson-Cook (J-C) material model with the Grüneisen equation of state (MAT_015 and EOS_GRUNEISEN accordingly). In addition, we make use of stress propagation into target thickness to analyze the origin of different points on the Back Face Velocity (BFV) profile during shock propagation. Finally, we provide evidence that 2D compressive effects do not depend only on the focal spot size or target thickness such as the edge effects but also on power density and material initial yield strength.

© 2022 Author(s). All article content, except where otherwise noted, is licensed under a Creative Commons Attribution (CC BY) license (http://creativecommons.org/licenses/by/4.0/). https://doi.org/10.1063/5.0080326

I. INTRODUCTION

Applications using high strain rate laser shock is continuously developing in the last decade. Laser shock is used for engineering applications, for example, Laser Shock Peening (LSP)[1–4] to enhance the resistance of materials to surface-related failures such as fatigue or corrosion.[5,6] This process introduces compressive residual stress fields at the surface through possible dislocations and grain refinement due to high strain rate hardening[7–9] and by doing so improves tribological performances. Another promising application is the laser adhesion test (LASAT),[10,11] where researchers evaluate the bonding strength in stack of laminates Carbon Fiber Reinforced Polymer (CFRP) by identifying the tensile stress areas due to high-power laser impact. We can also mention Laser Impact Welding (LIW)[12] and laser paint stripping.[13,14]

During a laser shock, a shock wave is generated and propagates through the target. It is formed due to the expansion of a high pressure plasma produced by laser (intensity order of GW/cm^2) pulse in the range of ns duration[15] as shown in Fig. 1. Moreover, Anderholm proved that it was possible to increase the pressure delivered through a laser shock up to six times compared

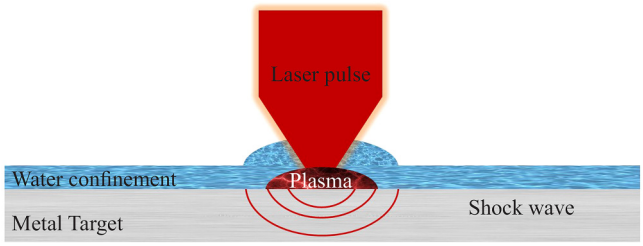

FIG. 1. Schematic setup of the laser shock experiment under a water confined regime (WCR).

to the direct configuration by confining the plasma using any transparent medium to the laser wavelength[16,17] such as water[15,18] or solid polymers[19,20] for the same laser intensity.

The wide range of parameters (related to material properties, laser parameters, and overlapping configuration) require process optimization using numerical twin modeling. For example, Ballard developed a one-dimensional approach where the transition between the elastic and plastic parts of the wave is marked by the elastic precursor due to a decrease in the wave velocity in the plastic part.[21] The author used this approach to study the influence of strain hardening and viscoplasticity on wave propagation. Furthermore, different finite element commercial codes have been used to reproduce shock wave propagation under laser impact such as ABAQUS[1,19,22] or the non-linear explicit code LS-DYNA.[23–26] These simulations allow to demonstrate edge effects affecting shock wave propagation and stress fields in the material.[27] They are very sensitive to boundary conditions (spatial and temporal pressure profiles) and mechanical properties.

Recently, many works investigated the ablation pressure in the confined regime.[15,19,28,29] Notably, Scius-Bertrand *et al.*[15] collected an extensive range of experimental data to validate 1D ESTHER code[30] given plasma microscopic parameters like temperature and density. The authors provide also scaling laws for the temporal pressure profile that can be used as loading conditions to simulate the process with mechanical codes. Furthermore, Rondepierre *et al.* conducted in-depth investigations of plasma pressure as a function of laser spot size to underline the importance of the multi-dimensional release of the plasma for submillimeter laser spot sizes.[29] The authors extended Fabbro's model[28] with a new scaling law depending on power density and spot diameter. In both models, progress was done to control laser loading through the real top hat spatial profile, energy, and pulse profiles measurement shot by shot.

This article aims to link material behavior under such shocks and usage of these new advances on pressure produced by the confined regime. The objective is to discriminate the impact of loading parameters (spatial and temporal) from mechanical behavior of the material. Comprehensive approach using simulation is based on modeling from the Johnson-Cook (J-C) model implemented in multidimensional LS-DYNA software and uniaxial elastic plastic approaches to highlight the main mechanism through literature parameters.

To have a general approach, first pure aluminum (pure-AL) is investigated by focusing on spatial loading conditions affecting shock propagation. To that scope, uniaxial and multiaxial models are described in Secs. II A and II B accordingly. In Sec. III, experimental setup to measure the Back Face Velocity (BFV) of aluminum alloys under laser shock is described for new sets of experiments with various well-controlled laser parameters. Furthermore, loading conditions used in numerical simulations (temporal and spatial loading conditions) are discussed in Sec. IV. Thereafter, we simulate the laser shock propagation through a pure-AL plate using a uniaxial approach (Sec. V A) and beyond (Sec. V B), where we analyze the related 2D phenomena and their signature on the dynamic response of the target. Finally, we validate and optimize our numerical results on pure-AL and Aluminum 2024-T3 (AA2024-T3) accordingly using the Velocity Interferometer System for Any Reflector (VISAR) to measure the BFV, which has been done in Hephaïstos Laser facility located in the PIMM laboratory (Procédés et Ingénierie en Mécanique et Matériaux) as presented in Sec. V C. We discuss the obtained results in Sec. VI and conclude in Sec. VII.

II. ONE-DIMENSIONAL AND MULTIDIMENSIONAL MODEL

Laser shock propagation is characterized by high strain rate deformation ($10^6\ s^{-1}$), short load impulse (few tens of ns), and strong stress (GPa), which makes it difficult to analyze the background of the physical mechanisms. Therefore, numerical simulation could provide the detailed phenomena and analyze the stress propagation during laser shock propagation. Starting with the uniaxial approach in Sec. II A, we present the numerical method used to derive the stress wave propagation. Thereafter, we utilized LS-DYNA to analyze the contribution of a multidimensional model on the dynamical results with respect to the uniaxial approach within Sec. II B.

A. Uniaxial approach

1. Problem statement

We assume here that the total strain field is uniaxial, which reduces the behavior of the material at the center of the impact, and along the impact direction. By deliberately excluding a 2D description in this approach, we aim to assess the importance of 2D effects in the behavior of the impacted specimen, with respect to other effects from plasticity. Due to the amplitudes of the stress waves generated by the laser during the LSP process, the propagation of the waves occurs both elastically and plastically. According to the literature works,[21,31,32] plasticity alone can induce specific propagation behaviors, since a shockwave travels at a lower speed while it induces plasticity in the material than when it does not, making the elastic and plastic parts of the wave interact with each other.

2. Modeling of the elastic-plastic propagation

Elastic propagation: When considering a purely elastic evolution (the increment of plastic strain is zero) in a homogeneous isotropic material, and for a uniaxial state of strain, the stress wave propagation is governed by the following equation (the

developments can be found in Appendix A):

$$\frac{\partial \boldsymbol{U}}{\partial t} + \boldsymbol{A} \times \frac{\partial \boldsymbol{U}}{\partial x_1} = 0. \tag{1}$$

In Eq. (1), x_1 is the coordinate in the direction of the shock, and $\boldsymbol{U}$ and $\boldsymbol{A}$ are defined in the following equation:

$$\boldsymbol{U} = \begin{pmatrix} \sigma_{11} \\ v_1 \end{pmatrix}, \quad \boldsymbol{A} = \begin{pmatrix} 0 & -\left(\kappa + \frac{4}{3}\mu\right) \\ -\frac{1}{\rho} & 0 \end{pmatrix}. \tag{2}$$

σ_{11} is the axial component of the stress tensor in the direction of the shock and v_1 is the material velocity component in the same direction, such that $v_1 = \partial u_1/\partial t$, with u_1 being the axial displacement component. In matrix $\boldsymbol{A}$, ρ refers to the density of the material, while κ and μ are the bulk and shear moduli, respectively. The derivation of Eq. (1) needs the assumption of a standard elastic behavior using Hooke's Law, instead of a hydrodynamic description via an Equation of State. According to Ballard,[21] the hydrodynamic behavior can be neglected as a first approximation if the applied pressure is under 0.1κ. We will check that the applications follow this condition.

Plastic correction: In the case of a plastic behavior, the plastic strain increment $\dot{\boldsymbol{\varepsilon}}_p$ is non zero. In our case, plasticity is detected when the equivalent von Mises stress exceeds the plastic flow stress, given here by the Johnson-Cook isotropic hardening model,[33]

$$R(\bar{\boldsymbol{\varepsilon}}_p, \dot{\bar{\boldsymbol{\varepsilon}}}_p) = \left(A + B\bar{\boldsymbol{\varepsilon}}_p^n\right)\left(1 + C\ln\left(\frac{\dot{\bar{\boldsymbol{\varepsilon}}}_p}{\dot{\varepsilon}_0}\right)\right) \times \left(1 - \left(\frac{T - T_0}{T_m - T_0}\right)^m\right), \tag{3}$$

where A is the initial yield strength of the material at the quasi-static strain rate; B and n are the strain hardening modulus and exponent, respectively; C is the strain rate sensitivity parameter; m is the thermal softening coefficient; T is temperature; and T_0 and T_m are the reference and melting temperatures accordingly. In the following, the influence of the temperature will be neglected ($T = T_0$).[34–36] $\dot{\boldsymbol{\varepsilon}}_0$ is the reference plastic strain rate, and $\bar{\boldsymbol{\varepsilon}}_p$ is the equivalent strain defined as

$$\bar{\boldsymbol{\varepsilon}}_p = \int_0^t \sqrt{\frac{2}{3}\dot{\boldsymbol{\varepsilon}}_p : \dot{\boldsymbol{\varepsilon}}_p}\, dt. \tag{4}$$

In Eq. (4), we introduce the notation " : " for the double dot product, which can be defined as follows:

$$\boldsymbol{a} : \boldsymbol{b} = \sum_{i,j} a_{ij} b_{ij}, \tag{5}$$

where $\boldsymbol{a}$ and $\boldsymbol{b}$ are second-order tensors. We also introduce the accumulated plastic strain p, such that its rate follows the equation:

$$\dot{p} = \sqrt{\frac{2}{3}\dot{\boldsymbol{\varepsilon}}_p : \dot{\boldsymbol{\varepsilon}}_p}. \tag{6}$$

We can, thus, define the yield function as

$$g = \sigma^{vM} - R(\bar{\boldsymbol{\varepsilon}}_p, \dot{\bar{\boldsymbol{\varepsilon}}}_p), \tag{7}$$

σ^{vM} referring to the von Mises equivalent stress or the 2nd invariant of the stress tensor: $\sigma^{vM} = J_2(\boldsymbol{\sigma}) = \sqrt{\frac{3}{2}\boldsymbol{S} : \boldsymbol{S}}$, with $\boldsymbol{S}$ being the deviatoric part of the stress tensor, such that $\boldsymbol{S} = \boldsymbol{\sigma} - \frac{1}{3}\mathrm{Tr}(\boldsymbol{\sigma})\boldsymbol{I}$. The plastic correction ensures that the flow rule and consistency conditions hold,

$$\begin{cases} \dot{\boldsymbol{\varepsilon}}^p = \dot{\Lambda}\frac{\partial g}{\partial \boldsymbol{\sigma}} \\ \dot{\Lambda} \geq 0 \\ \dot{\Lambda} g = 0 \end{cases}, \tag{8}$$

where Λ is the so-called plastic multiplier. For the von Mises criterion, it can be derived that $\dot{\Lambda} = \dot{p}$.

The Johnson-Cook model is highly non-linear, which implies that taking plasticity into account, even for a uniaxial problem is not straightforward. We proceed by using a radial return algorithm, following the strategies of works from the literature,[37,38] coupled with a fixed point iteration updating the internal variables. This last part ensures that the new flow strength is updated at each iteration and, thus, that the radial return is computed implicitly for the value of the flow stress of the current iteration. The global numerical resolution proceeds as follows: at each time step and for each cell of the discretized numerical domain, an elastic trial state is computed by solving Eq. (1). From the latter, the yield function g from Eq. (7) is evaluated. If $g \leq 0$, then the step is elastic and one can proceed to the next time step. If not, one must apply a correction on the stress and compute the plastic strain increment such that the flow rule and consistency conditions are verified. Here, this problem requires to solve a non-linear equation to find the correct value of the accumulated plastic strain rate, for which root-finding methods can be used. The steps taken to compute the state of the system at the next time increment are summarized in the pseudo-code algorithm given in Appendix B.

3. Numerical method for the stress wave propagation

The differential equation we need to solve is Eq. (1). The problem was specifically put in this hyperbolic form to allow the use of dedicated precise numerical methods. Following the literature works,[32,39] we use a Godunov-type with a high resolution method. The details of the method can be found in the work of Leveque.[40] Such a method is well-suited for rapid loadings, such as the ones typical of the LSP process, because it is able to limit the spurious oscillations appearing in the solution without adding too much artificial viscosity.

B. Multidimensional model

Non-linear finite element solver LS-DYNA has been used to simulate the material response under laser shock. Similar problems have been already solved using this code such as hypervelocity, ballistic impacts,[41,42] and laser shock propagation in composite.[23] Authors studied dynamic behavior of materials under high strain rate loading conditions using different types of material

model.[33,43,44] Moreover, an equation of state is necessary to provide the thermodynamic relation relying the sudden pressure, internal energy, and density changes during the shock wave.[41] Following parts present the used 2D-axisymmetric numerical model, then the material model in LS-DYNA and the associated equation of state.

1. Mesh and geometry

During laser shock, the main interest is focused on the central zone in relation to pressure loading and the measuring plan of the Back Face Velocity (BFV) as shown in Fig. 2. Thereafter, a mesh has been generated using the Bias function to obtain thinner mesh at the center of the plate. The smaller shell element size is $1.85 \times 4\,\mu m^2$ for the 2D axisymmetric model, which is based on the revolution symmetry assumptions to reduce simulation time as well (Fig. 2).

2. Material model

Since we are dealing with a high strain rate (up to $10^6\ s^{-1}$), the material response will be significantly different from static to quasi-static and dynamic loading conditions.[45] To better describe strain rate effects, various high strain rate formulations have been used for laser shock in aerospace applications, such as Bammann model[43] and Zerilli–Armstrong material model in Ref. 44. An apt material model is the J-C model[33] owing to its availability in finite elements codes,[46] which is the function of Von Mises tensile flow stress, in accordance with strain hardening, strain rate hardening, and thermal softening as defined in Eq. (3). Different works have assumed negligible thermal effects during the laser shock process[34–36] and have provided validated results comparing to the experiment. The J-C (Johnson-Cook) material model is available in LS-DYNA in different forms; in this study, we use the MAT_JOHNSON_COOK (MAT_015) coupled with the equation of state. Following the methodology of the previous works, thermal effects will be assumed to be negligeable.

3. Equation of state

The Grüneisen is a commonly used Equation of State (EOS) in high strain rate impact.[47,48] It accurately represents the behavior of the Hugoniot relationships under shock compression. The Grüneisen as defined in LS-DYNA (EOS_GRUNEISEN) with cubic shock-velocity as a function of particle velocity $v_s(v_p)$ defines different pressures for compressed and extended materials as the following equations accordingly:

$$p = \frac{\rho_0 C^2 \beta\left[1 + \left(1 - \frac{\gamma_0}{2}\right)\beta - \frac{a}{2}\beta^2\right]}{\left[1 - (S_1 - 1)\beta - S_2 \frac{\beta^2}{\beta+1} - S_3 \frac{\beta^3}{(\beta+1)^2}\right]^2} + (\gamma_0 + a\beta)E, \tag{9a}$$

$$p = \rho_0 C^2 \beta + (\gamma_0 + a\beta)E. \tag{9b}$$

Here, C is the intercept of the $v_s(v_p)$ curve (value of v_s when $v_p = 0$[49]); S_1, S_2, and S_3 are the unitless coefficients of the slope of the $v_s(v_p)$ curve; γ_0 is the unitless Grüneisen gamma, a is the unitless, first-order volume correction to γ_0, and $\beta = \frac{\rho}{\rho_0} - 1$, E denotes the internal energy.

III. EXPERIMENTAL SETUP

A. Used laser systems and optical setup

Experiments have been performed on Hephaistos facility at PIMM laboratory. The laser system (a GAIA HP, from Thales) delivers a Gaussian temporal pulse of 7.2 ns duration at Full Width at Half Maximum (FWHM) in the green visible wavelength (532 nm) and with an energy going up to 14 J. Finally, a motorized half-wave plate is used and coupled to a polarizer to control the laser energy emission on target. Pulse durations and energies were

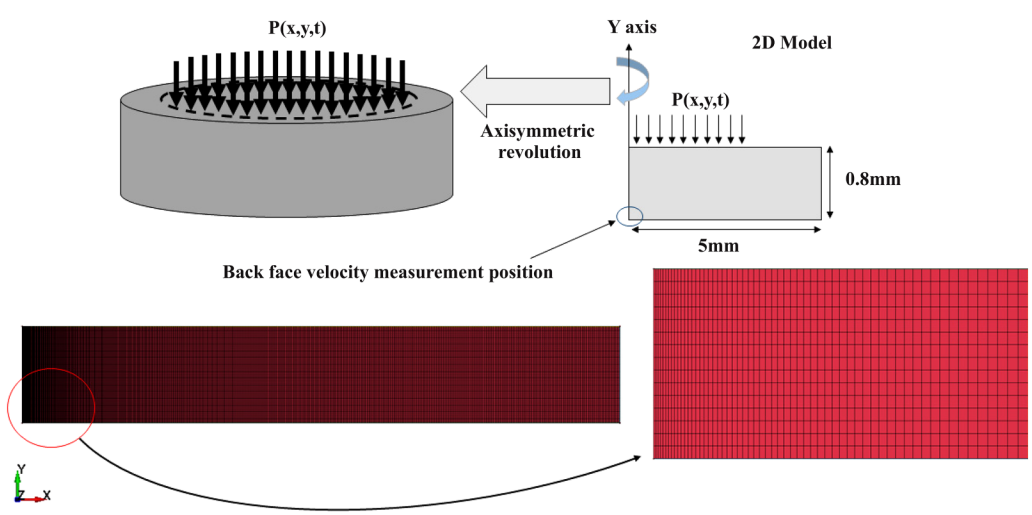

FIG. 2. 2D axisymmetric model with a 311 250 shell elements.

measured, respectively, pulse by pulse with a DET-10A2 (Thorlabs) photodiode and a QE50LP (Gentec-EO, Canada) calorimeter (calibrated by a second calorimeter every day of shot campaign). The laser beam was focused on the metal target and smoothened using a DOE (Diffractive Optical Element) coupled to an appropriate converging lens in order to obtain a focal spot size ranging from 2 to 5 mm. Top-hat beam profiles on the target were obtained, as shown in Fig. 6, and measured through a Basler-ac camera (pixel size : $5.5 \times 5.5\,\mu$m) located at the target surface.

B. Velocity measurement with the VISAR system

Back free surface velocity time resolved profiles of the target are measured by a Velocity Interferometer System for Any Reflector (VISAR) based on a Barker system.[50,51] It gives the signature of shock waves and its dependence on the target. The resolution of less than 1 ns is achieved; thus, the elastic precursor velocity can be measured as well.

As shown in Fig. 3, a VISAR is constituted of two parts:

- A single longitudinal mode (λ_0 with a narrow spectral width) collimated laser beam (Verdi CW 532 nm made by Coherent) is focused on the rear surface of the metal target. The scattered reflection of the beam is then collected and directed toward the second part to be analyzed; a short focal length has to be used to collect as much light as possible. This reflection is wavelength-shifted according to Doppler-Fizeau's effect as the surface is moving under a velocity V,

$$\lambda(t) = \lambda_0\left(1 - \frac{V(t)}{c}\right), \tag{10}$$

with c being the speed of light in vacuum.
- The second part is a field-compensated Michelson-like interferometer. Calibrated mirror enables to delay one arm from the other of the interferometer. It changes the initial path difference (δ) in the interferometer, and hence, the required velocity to move from one fringe to the next one is also changed: this is the Velocity Per Fringe (VPF) factor. Then, the interference between the signal at time t [wavelength $\lambda(t)$] and one at time $t + \Delta t$ [wavelength $\lambda(t + \Delta t)$] is produced. Therefore, there is a translation of the interference fringes as soon as a wavelength-shift occurs. Fringes are acquired by using two fast PhotoMultipliers (PM provided by Valyn company).

Time-resolved measurement of the interference intensity enables one to obtain the corresponding velocity by the current equation,

$$I_v(t) \propto 1 + cos\left(\frac{2\pi\delta c}{\lambda_0(c - V(t))}\right). \tag{11}$$

C. Target materials

This study is based on the simulation of shock wave propagation within pure-AL and AA2024-T3. Their current mechanical properties and material model J-C parameters as elaborated in Eq. (3) have been collected from different works in the literature[34,52–54] as summarized in Tables I and II.

Where ρ refers to the density, μ refers to the shear modulus, C_p is the specific heat capacity, and the rest of parameters has been defined in Eq. (3).

IV. PRESSURE LOADING MODELING

This part presents the source term used in our simulations for the laser-induced plasma pressure (temporal and spatial input).

On the one hand, the temporal distribution of the pressure has to be defined. This has been done using previous models based on numerical simulations and experimental fitting.[15,29,30] On the other hand, the spatial distribution of the pressure along the laser

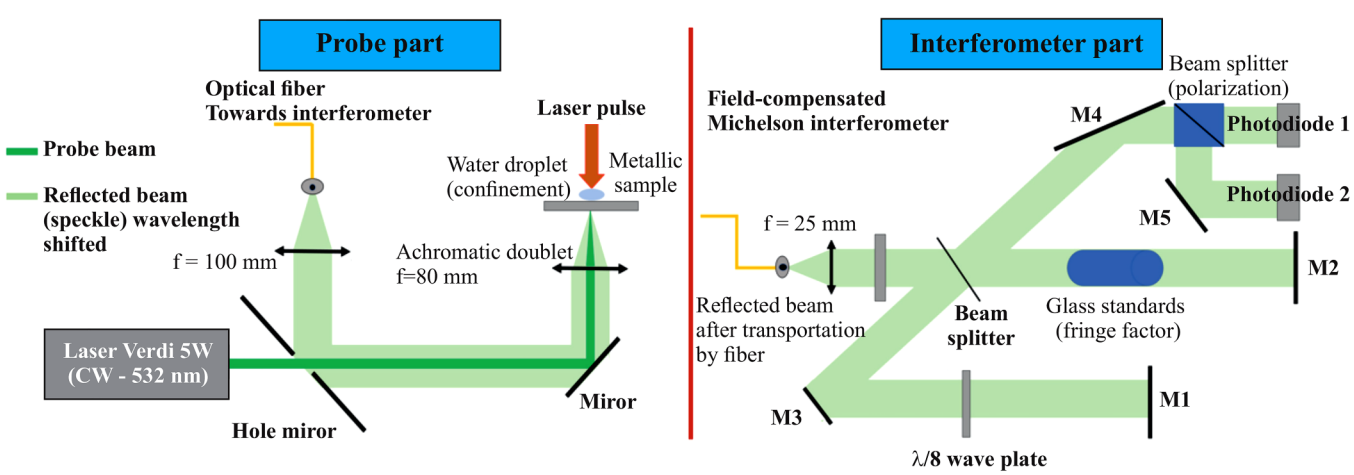

FIG. 3. VISAR setup used for rear-free surface velocity measurements.

TABLE I. Mechanical properties for pure-AL and AA2024-T3.[54]

Material	ρ(kg/m^3)	μ(GPa)	C_p(J/g-°C)	T_m(°C)	T_0(°C)
Pure-AL	2698.9	25	0.9	660.37	25
2024-T3	2780	28	0.875	502	25

spot irradiating the metal target is defined using experimental measurements of the spatial distribution of power density. A proportional scale law is directly applied between the power density distribution and the pressure distribution, as the maximum reached pressure (P_{max} in GPa) is given by the following experimental law [expression (12)]:

$$P_{max} = 2.2\sqrt{I_{laser}}, \tag{12}$$

where I_{laser} is the power density in GW/cm^2; this formula has been fitted in the function of laser intensities based on the original formula[55] by using $\alpha = 0.6$.[56]

A. Temporal pressure distribution

Most recent pressure time-resolved profiles from literature have been implemented. For earliest plasma period corresponding up to the end of the laser pulse, we use scale law extracted from ESTHER code.[15] For longer periods of time, Rondepierre *et al.* demonstrated that the release depends on focal spots through the plasma expansion behavior.[29] Indeed, rarefaction phenomenon is dominant when the blast wave reaches the center of the plasma.[29]

1. Description of the rarefaction phenomenon

Following the work of Pirri in 1973,[57] a rarefaction wave propagates from the edges of the laser spot toward its center, in reaction to the radial expansion of the plasma. This rarefaction wave is assumed to travel at the local speed of sound C_s. As the plasma is considered as an ideal gas, the speed of sound is given by the following equation:

$$C_s = \sqrt{\frac{\gamma P}{\rho}} = \sqrt{\frac{\gamma R T_p}{M}}, \tag{13}$$

with γ being the adiabatic coefficient, P being the pressure, ρ being the density, R being the gas constant, T_p being the plasma temperature, and M being the molar mass.

One can calculate the time τ_R from which the rarefaction wave reaches the center of the plasma to impact its release as in the following equation:

$$\tau_R = \frac{D}{2C_{s,m}}, \tag{14}$$

with D being the laser spot diameter and $C_{s,m}$ being the average sound of speed (from $t = 0$ to $t = \tau_R$) regarding the drop in the plasma temperature.

From this time, the plasma pressure on the surface is affected by a spherical blast wave, and the pressure starts to follow a scaling law (as shown in Fig. 5), which is given by the following equation:

$$P(t) \propto \left(\frac{t}{\tau_R}\right)^{-\frac{6}{5}}. \tag{15}$$

2. Calculation of τ_R

To implement the rarefaction phenomena in our pressure temporal profile, we have to calculate the time τ_R from which to apply the rarefaction scaling law on the pressure.

Either the density or the molar mass of the plasma cannot be easily calculated (the plasma is partially made of ionized water, from the confinement) to obtain the average speed of sound $C_{s,m}$. Therefore, to calculate τ_R, we made the choice of using the maximum reached temperature T_M, associated to a maximum speed of sound $C_{M,s}$. Thus, the speed of sound is obtained at any time by applying a proportional ratio from these maximum values according to the following expression:

$$C_s(t) = C_{M,s}\sqrt{\frac{T_p(t)}{T_M}}. \tag{16}$$

From numerical simulations (Esther Code, CEA[30]), the maximum temperature T_M was estimated to be around 50 000 K for a power density of $I_0 = 4\,\mathrm{GW/cm^2}$, which is also consistent with experimental results from Ref. 58 ($T_M \approx 8000$ K at $0.4\,\mathrm{GW/cm^2}$). This also gives $C_{M,s} \approx 11\,000$ m/s at I_0.

TABLE II. Jonshon Cook parameters of pure-AL and AA2024-T3[52] and Grüneisen parameters.[48]

Material	A(MPa)	B(MPa)	C	n	C(m/s)	S_1	γ_0
Pure-AL	90	200	0.035	0.3	5328	1.338	2
2024-T3	369	329	0.025	0.35	5328	1.338	2

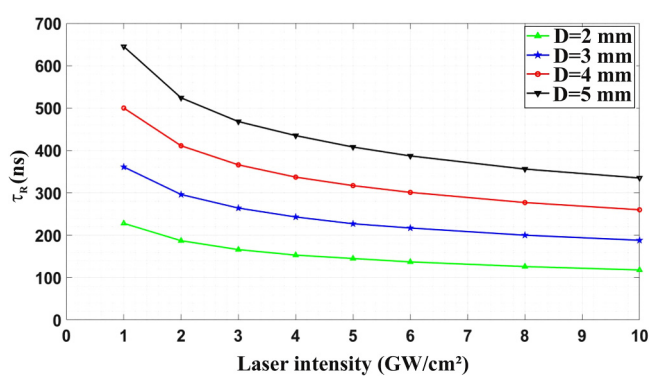

FIG. 4. Values of the rarefaction time τ_R (ns) as a function of the power density I (GW/cm^2) for different laser spot sizes.

Furthermore, as the plasma is considered to be an ideal gas, we also assumed that the maximum temperature, similarly to the maximum pressure [see expression (12)], is proportional to the intensity: $T_M \propto \sqrt{I}$, so that

$$T_p(I) = T_p(I_0)\sqrt{\frac{I}{I_0}}. \tag{17}$$

The rarefaction time has been calculated as a function of the power density and for our four usually used laser spot sizes (2, 3, 4, and 5 mm), as shown in Fig. 4. The following law has been extracted to get the rarefaction time knowing the power density (I) and the laser spot size (D),

$$\tau_R(\mathrm{ns}) = \frac{aD(\mathrm{mm}) - b}{I^c(\mathrm{GW/cm^2})}, \tag{18}$$

where $a = 1380\,\mathrm{GW}^{c\sim}\mathrm{ns/cm}^{2c+1}$, $b = 52\,\mathrm{ns\,GW}^c/\mathrm{cm}^{2c}$, and $c = 0.285$.

As expected, this rarefaction time will be larger with bigger laser spot sizes (the distance to be travelled by the wave has increased) and smaller with higher laser intensities, since the initial temperature will be higher as well the speed of sound.

In our study, we combined the 1D profile provided by ESTHER code (the red curve PT1) and the rarefaction phenomenon for each power density (I) and focal spot (D) as showed in Fig. 5 by the green (PT2) and the blue (PT3) profiles, respectively, for 3 and 4 mm focal spot under 3 $\mathrm{GW/cm^2}$ power density.

B. Spatial pressure distribution

The power density is measured using a Basler-ac camera as shown in Fig. 6. The homogeneity of the focal spot is ensured thanks to the use of a DOE (Diffractive Optical Element) as shown by gray circles in Figs. 6(a) and 6(b) for 3 and 4 mm focal spots, respectively.

As illustrated in Fig. 6(c), the transformation between the spatial pressure profile of 3 and 4 mm focal spots are obtained by homothety of ratio SF = 1.315. This value corresponds to the ratio between the two Full Width at Half Maximum of the spatial profiles (FWHM1/FWHM2).

The fluctuation that exists in the spatial profile will make a huge loading gradient between one element and another even with 1 μm mesh size. These fluctuations are created due to the interferences of the laser beam after being diffracted by the DOE. However, this will be quickly homogenized during the plasma creation by plasma absorption in the conduction zone and the ablation front from critical density to solid surface. To avoid this power density variation and to reach the plasma pressure, we filter the experiment profile (SP1) using a second-order Butterworth filter at 0.455 kHz to obtain the smooth profile (SP2) shown as the blue curve in Fig. 8 for 3 and 4 mm focal spot diameter in (a) and (b) accordingly. Moreover, we filter the average profile of the experimental spatial pressure distribution with the first-order Butterworth filter at 1.82 kHz to obtain the sharp and the closer profile to the experimental profile shown as the green curve SP3 in Fig. 8, which highlights a strong boundary pressure gradient at the edge of the focal spot. We provide the analytical fittings of the spatial profile [I_r for SP2 and SP3 in Table IV (Appendix D)].

V. RESULTS

A comprehensive study of loading conditions such as the spatial and temporal power density distribution has been done first on a pure-AL target using Uniaxial and multidimensional simulations. For each parameter, BFV profiles are extracted to analyze experimental results in relation to physical phenomena. Furthermore, these numerical models are compared in Sec. V C with experimental results for pure-AL and calibrated for AA2024-T3.

A. Uniaxial results

Using the uniaxial approach described in Sec. II A, we calculated the Back Face Velocity (BFV) of pure-AL under laser impact of three different intensities (0.7, 1.8, and 3.3 $\mathrm{GW/cm^2}$) as

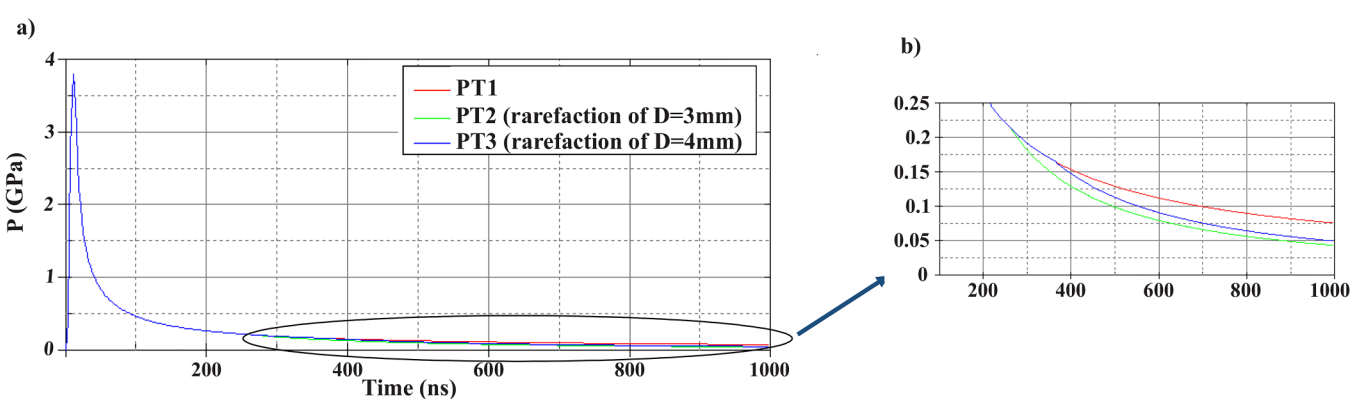

FIG. 5. Temporal pressure profile using the analytical fit of Scius-Bertrand *et al.*[15] in PT1, while for PT2 and PT3 we count also the rarefaction phenomena for 3 and 4 mm focal spot sizes accordingly as shown in (a) and (b).

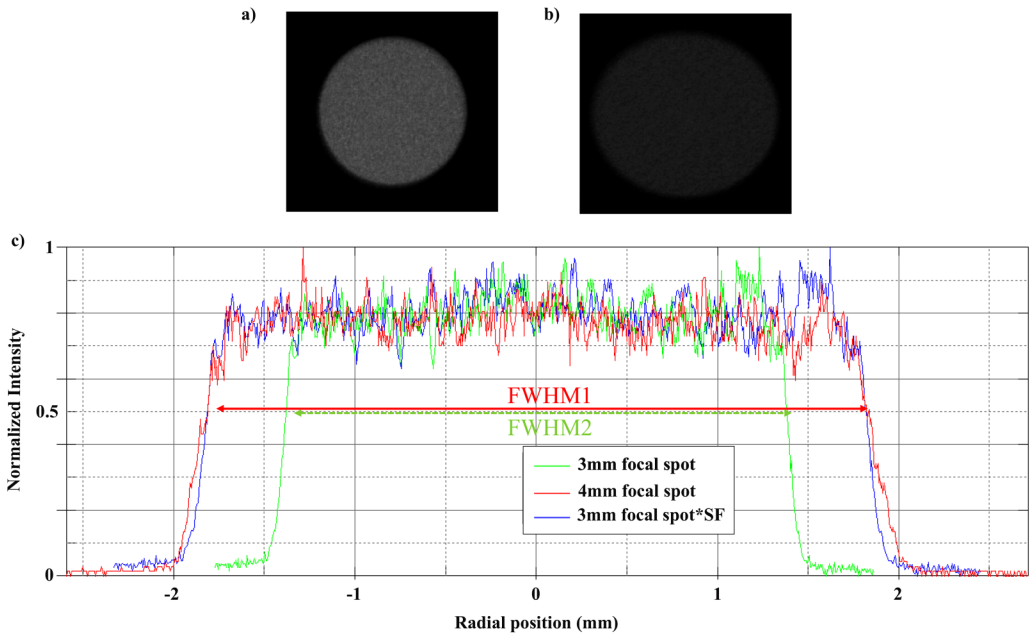

FIG. 6. CCD image of a 3 and 4 mm focal spot in (a) and (b) accordingly, with the associated normalized laser spatial intensity (green and red curves accordingly) in (c). The blue curve corresponds to the homothety of the green one using the scale factor (SF = 1.315).

illustrated in Fig. 7. In these cases, the maximum pressure, computed with Eq. (12), is under $0.1\kappa \approx 8$ GPa for the pure-Al. Here, the uniaxial approach is a valid approximation of the true behavior.

As shown in Fig. 7, the simulated BFV using the uniaxial approach shows the same behavior under different applied laser intensities, and the signature of stress propagation due to the laser shock on the simulated BFV is characterized by some points as summarized in Table III.

We can observe in Fig. 7 three main peaks (b, c, and d) for all laser loadings at 190, 500–550, and 800–900 ns, respectively. They correspond to the emergence of the shock wave after the propagation of incident shock wave through the target: one time and to

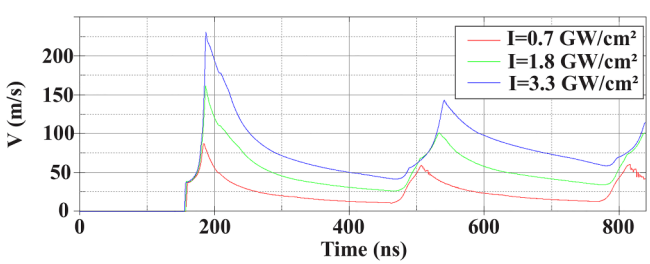

FIG. 7. BFV of 1 mm pure-AL plate under three laser intensities 0.7, 1.8, and 3.3 GW/cm^2 calculated using a uniaxial approach as shown by red, green, and blue curves accordingly. Points a, b, c, and d are identified according to their origin in Table III.

going back and forth, respectively. As illustrated in Fig. 7, the sole description of the elasto-plastic state of pure-AL during the impact at its center is not enough to observe edge effects as explained by Berthe *et al.*,[11] which must then originate from the regions of the shockwave outside of its center. Hence, the current 1D model cannot be useful for the LASAT application (which need to take into consideration edge effects) contrary to the multidimensional models that are described in Sec. V B.

B. Multidimensional results

In order to take into account the multidimensional effects on the BFV during the laser shock, we are going to use the multiphysics solver LS-DYNA to analyze the influence of spatial and temporal loading conditions on the BFV profile.

1. Influence of loading conditions on BFV

The first step is to verify which type of spatial profile we can use to model our power density spatial distribution. To that scope, we simulate BFV of pure-AL using three types of spatial distribution (SP1, SP2, and SP3) for 3 mm focal spot as shown in Fig. 8. For material model parameters, we use literature parameters as summarized in Tables I and II, and for loading conditions, we use the analytical pressure profile developed using 1D ESTHER code[15] for 3 GW/cm^2 power density (PT1 in Fig. 5).

Figure 8 reveals that the BFV profile simulated using the measured experimental spatial distribution of the power density SP1 [black curve in Fig. 8(a)] provides a lot of fluctuations due to the

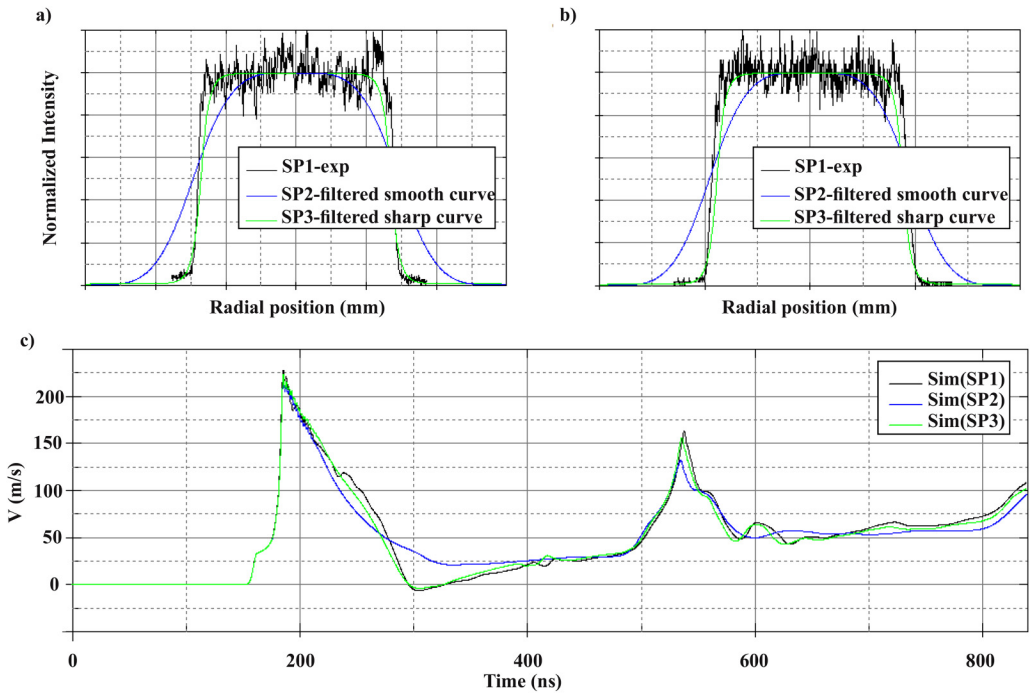

FIG. 8. Spatial distribution of normalized intensity profiles SP1, SP2, and SP3 for 3 and 4 mm focal spots in (a) and (b) accordingly, and the computed BFV of pure-AL under 3 GW/cm^2 power density using the three different spatial distribution profiles SP1, SP2, and SP3 for 3 mm focal spot (a) as shown by the curves **Sim(SP1)**, **Sim (SP2)**, and **Sim(SP3)** accordingly in (c).

one that already exist in the spatial profile SP1 as shown by the black curve **Sim(SP1)** in Fig. 8(c). Moreover, using SP2 [blue curve in Fig. 8(a)], smoothed BFV is obtained as shown by the blue curve **Sim(SP2)** in Fig. 8(c). However, the smoothed profile SP3 still provides some fluctuations on the BFV [**Sim(SP3)** in Fig. 8(c)], which could be related to the high gradient of pressure at the edge of the focal spot (where the energy decreases from 100% to 1% by moving 1.8 mm away from the focal center for 3 mm focal spot). To compromise, in the following simulation, we are going to use both spatial profiles (SP2 and SP3) but with the same 2D mesh developed in Fig. 2. Moreover, BFV profiles simulated with the experimental spatial profile or the sharp spatial profile (SP1 and SP3 accordingly) provide negative velocity after the first shock breaking out, which is related to the edge effects that cannot be reproduced by the smoothed spatial profile SP2 [green curve **Sim (SP2)** in Fig. 8(c)].

After choosing SP2 and SP3 as spatial pressure distributions, we analyzed the influence of the temporal pressure profile on the BFV. To that scope, we are going to simulate the BFV of pure-AL under 3 GW/cm^2 power density with 3 mm focal spot size [SP2 and SP3 from Fig. 8(a)] using PT1 (the 1D profile from Fig. 5 obtained using ESTHER[15]) as a reference to see the effect of rarefaction phenomena by using PT2 for 3 mm focal spot size (green curve in Fig. 5).

Figure 9 highlights the influence of counting the rarefaction phenomena in the loading conditions (where the blast wave arrives at the plasma center around 265 ns for a 3 mm focal spot) on the BFV. Influence of rarefaction phenomenon is negligible for our study as we see in Figs. 9(a) and 9(b), since we are looking only to the first three back and forth of the shock wave in the target. This influence will be more important for smaller focal spot and higher laser intensities according to Eq. (18). In the sequel, we are going to use the PT2 and PT3 as the temporal pressure distribution profile for the 3 and 4 mm focal spots accordingly.

2. Edge and compressive 2D effects

One of the current challenges is to identify which configurations trigger maximum tensile stresses in the samples that can result in debonding as the one used for the LASAT application[23] or paint stripping.[13] Edge effects are one of the interesting phenomena to understand and control their appearance under laser shock in order to allow the creation of regular spallation inside the material.[11,27] Authors proved that depending on the ratio thickness/laser spot diameter (=R), it is possible to stimulate edge effects and to generate tension or regular spallation inside the target.[11,27] In this part, we elaborate the edge and the compressive 2D effects, associating them to the BFV profile. For completeness, we analyze the sensitivity of these effects on the loading conditions and target properties.

Edge effects. As already shown in Fig. 8, the spatial distribution of the power density profile has a crucial role in the significance of

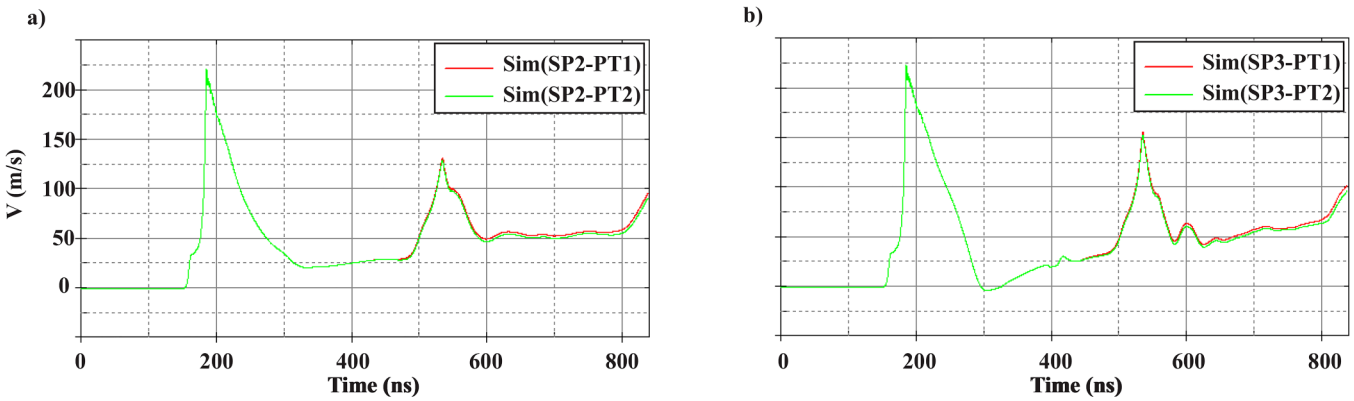

FIG. 9. BFV of pure-AL under 3 GW/cm^2 power density using two different spatial distribution profiles SP2 and SP3 for 3 mm spot diameter from Fig. 8(a) in (a) and (b) accordingly with different temporal profiles PT1 and PT2 from Fig. 5.

the edge effect that is present directly after the release of the 1st shock wave. The smallest edge effect is obtained for the smoothed profile SP2 as shown by the blue curve **Sim(SP2)** in Fig. 8(c). To analyze the origin of these effects during the shock wave propagation, we used the X-T diagram that provides us the axial stress level σ_{yy} distribution through the target thickness as shown in Fig. 10 and the associated BFV profile calculated using the sharp spatial profile SP3. We focus on σ_{yy} to analyze the axial response of targets, while the components σ_{xy} have been found to be negligible compared to the axial one at the back face. Indeed, the center of the stress wave deforms the material uniformly in compression/tension, hence the absence of any substantial shear stress.

Figure 10 reveals the link between the BFV profile and the stress level σ_{yy} through the thickness of the target due to the laser shock. Furthermore, the blue arrows show the propagation of the compression waves through the plate thickness which hit the back face and reflect as tensile waves as shown in the red arrows in Fig. 10. The signature of the elastic precursor on the BFV profile can be also linked to the separation of two compression waves that hit the back face, where the faster elastic one is marked by the dark circle in the X-T diagram (Fig. 10), while the plastic compression wave hits the back face and produces the first peak of the BFV profile (first shock).

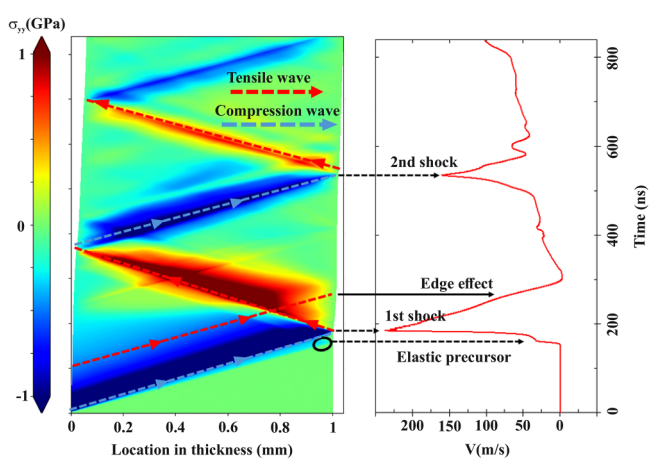

FIG. 10. Axial compression and tension stress level σ_{yy} (blue and red arrows accordingly) during the wave propagation through the target thickness (horizontal axis) and during the laser shock with the associated BFV profile under 3.3 GW/cm^2 power density and 3 mm focal spot (SP3).

In order to verify the influence of the ratio thickness/laser spot diameter (=R) on the edge effects (tensile 2D effects), different simulations have been done on 1 mm pure-AL thickness for different focal spot sizes under two different power densities (0.8 and 2 GW/cm^2) in Figs. 11(a) and 11(b) accordingly.

Figure 11 demonstrates that the first edge effect present in the first release after the first shock will be neglected at a ratio of R = 0.15 between the thickness and the focal spot diameter. In addition, the second edge effect needs a smaller ratio to be negligible (R = 0.095). Moreover, these ratios proved to be insensitive to the applied power density by comparing the sensitivity study of the BFV profile in Fig. 11(a) to the one in Fig. 11(b) under a different power density.

Compressive 2D effects. After analyzing the edge effects that are produced by a traction stress (red color) on the back face, we are going to analyze the third peak that appears on the BFV profile of pure-AL under 0.8 GW/cm^2 [red curve in Fig. 11(a)] and does not exist under 2 GW/cm^2 [red curve in Fig. 11(b)]. To that scope, we generate the X-T diagram of the 1 mm pure-AL under 0.7 GW/cm^2 as depicted in Fig. 12.

Figure 12 identifies the compression wave that is responsible for the third peak in the BFV profile of 1 mm pure-AL under 0.7 GW/cm^2. We mark three interesting points on the X-T diagram of σ_{yy} [E, F, and G in Fig. 12(a)]. Their corresponding BFV profile and σ_{yy} contours are given in Figs. 12(c) and 12(c) accordingly. In particular, we show the origin of this compression wave that has been noticed to be related to 2D effects propagating from the right and left sides of the sample [as shown in the σ_{yy} contours in Fig. 12(b)]. At point E, a 2D shock wave has been

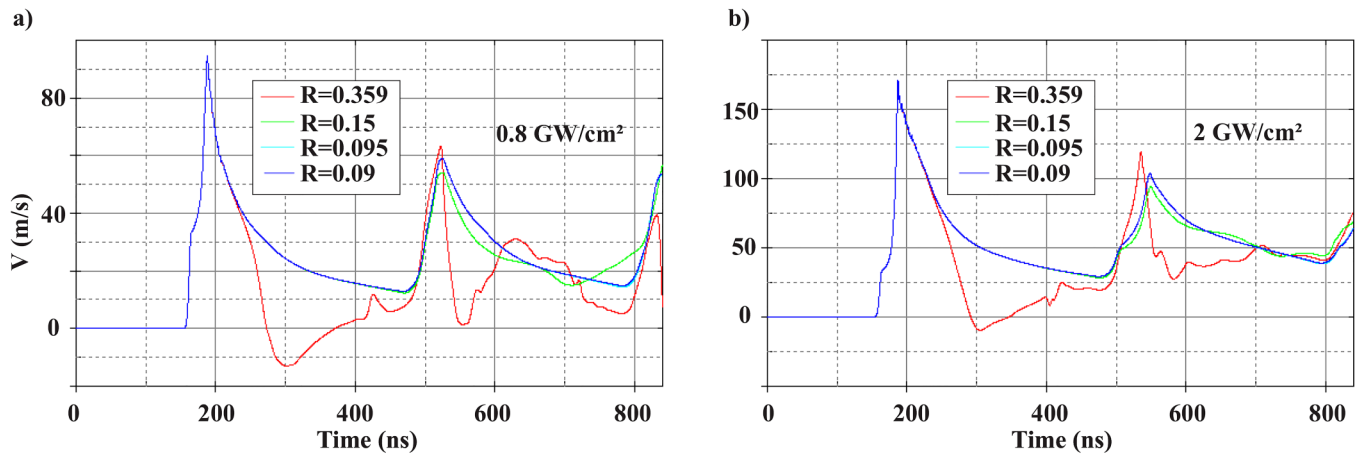

FIG. 11. Influence of the ratio thickness/focal spot diameter (=R) on edge effects for pure-AL of 1 mm thickness under different laser intensities, 0.8 and 2 GW/cm^2 in (a) and (b) accordingly.

generated and is going toward the back face that can be almost seen in the X-T diagram in Fig. 12(a). These 2D waves will reflect on the back face as a tensile wave and propagate towards the front face and reflect again as a compression wave [as shown by the contours plots of σ_{yy} in Fig. 12(c) for point F], another 2D wave will join the last one and propagate until they reach the back face and produce the third peak (point G) in the BFV profile [Fig. 12(b)].

It has been seen in Fig. 11 that compressive 2D effects will disappear also for a small ratio between thickness and laser spot diameter (R≤0.15). These 2D effects do not exist in Fig. 11(b) even for big ratio between thickness and laser spot diameter under 2 GW/cm^2 of power density. In order to verify the influence of applied pressure on these compressive 2D effects, we quantified the 2D velocity as noted in Fig. 12(b) with respect to the ratio between the applied laser pressure and pure-AL Hugoniot elastic limit pressure P_{HEL} as defined in the following equation:[5]

$$P_{HEL} = \frac{1}{2}\rho C_{el} V_F, \tag{19}$$

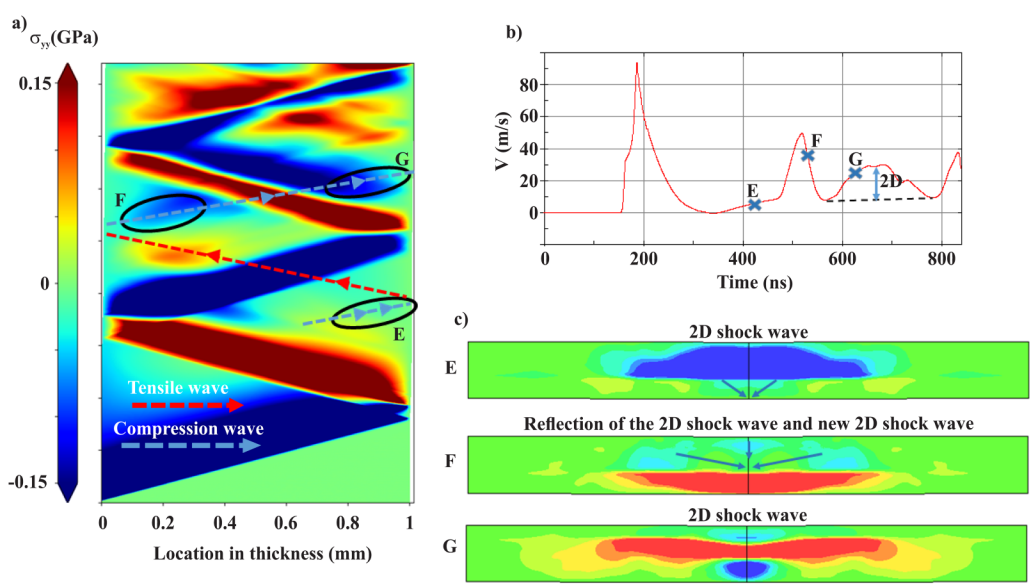

FIG. 12. Axial compression and tension stress level σ_{yy} (blue and red arrows accordingly) during the wave propagation through the target thickness (horizontal axis) under 0.7 GW/cm^2 in (a), with the associated BFV profile in (b), and σ_{yy} contours at three different points (E, F, and G) in (c).

where ρ is the material density, C_{el} is the elastic wave velocity given by Eq. (20), and V_F is the velocity that corresponds to the elastic precursor,

$$C_{el} = \sqrt{\frac{E(1-\nu)}{\rho(1+\nu)(1-2\nu)}}. \tag{20}$$

Using mechanical properties of the pure-AL[54] and its BFV profile under laser shock Fig. 12(b), we quantify the 2D velocity for different ratios between the laser applied pressure and the HEL one (P_{max}/P_{HEL}) using a 3 mm focal spot, a ratio of 13 is sufficient to neglect the compressive 2D effects. We note that for a larger focal spot diameter ($D > 3$ mm), this ratio between the applied laser pressure and the HEL one is more than enough to neglect the compressive 2D effects.

C. Experimental validation of numerical results

Apart from the different types of loadings that can be used in laser shock (spatial and pressure distribution), also different material model parameters are available in the literature. Therefore, experimental measurements of BFV should be done to validate our numerical inputs. Experimental laser shock has been operated on pure-AL with four different laser intensities according to the pressure ratio P_{max}/P_{HEL} in order to prove the relation between this later and the compressive 2D effects. To achieve that, we use 0.7, 1.8, 2.46, and 3.3 GW/cm^2 that correspond to a pressure ratio (P_{max}/P_{HEL}) of 6.13, 9.8, 11.5, and 13.3 accordingly, which will be compared with the numerical BFV as shown in Fig. 13. The BFV simulation of pure-AL is done with both filtered spatial power density distribution [SP2 and SP3 from Fig. 8(a)] and the modified temporal profile PT2 for a 3 mm focal spot (Fig. 5).

Figure 13 shows a good accordance between numerical and experimental results for pure-AL with different laser intensities applied. Two different spatial distribution of power density have been used, the sharp and the smoothed profile (SP2 and SP3) accordingly as illustrated in Fig. 8(a). BFV profiles calculated using the sharp profile [**Sim(SP3)**] reproduce very well the experimental velocity, especially the edge effects, while it was not been the case using the smoothed spatial profile [**Sim(SP2)**].

After validating the loading conditions in terms of pressure profiles using the pure-AL in Fig. 13, we compared the numerical BFV profile for AA2024-T3 with experimental measurements in Fig. 14 using a 4 mm focal spot in order to test the material model parameters that are summarized in Tables I and II.

Using the same intercept of the $v_s(v_p)$ curve of pure-AL for AA2024-T3 as summarized in Table II, the simulated wave does not reach the back face of the AA2024-T3 plate at the same time as the experimental wave reaches it see the cyan curve in Fig. 14 [**Sim(literature parameters)**]. To adjust the arrival time of the wave to the back face, the intercept of $v_s(v_p)$ in the Grüneisen equation of state

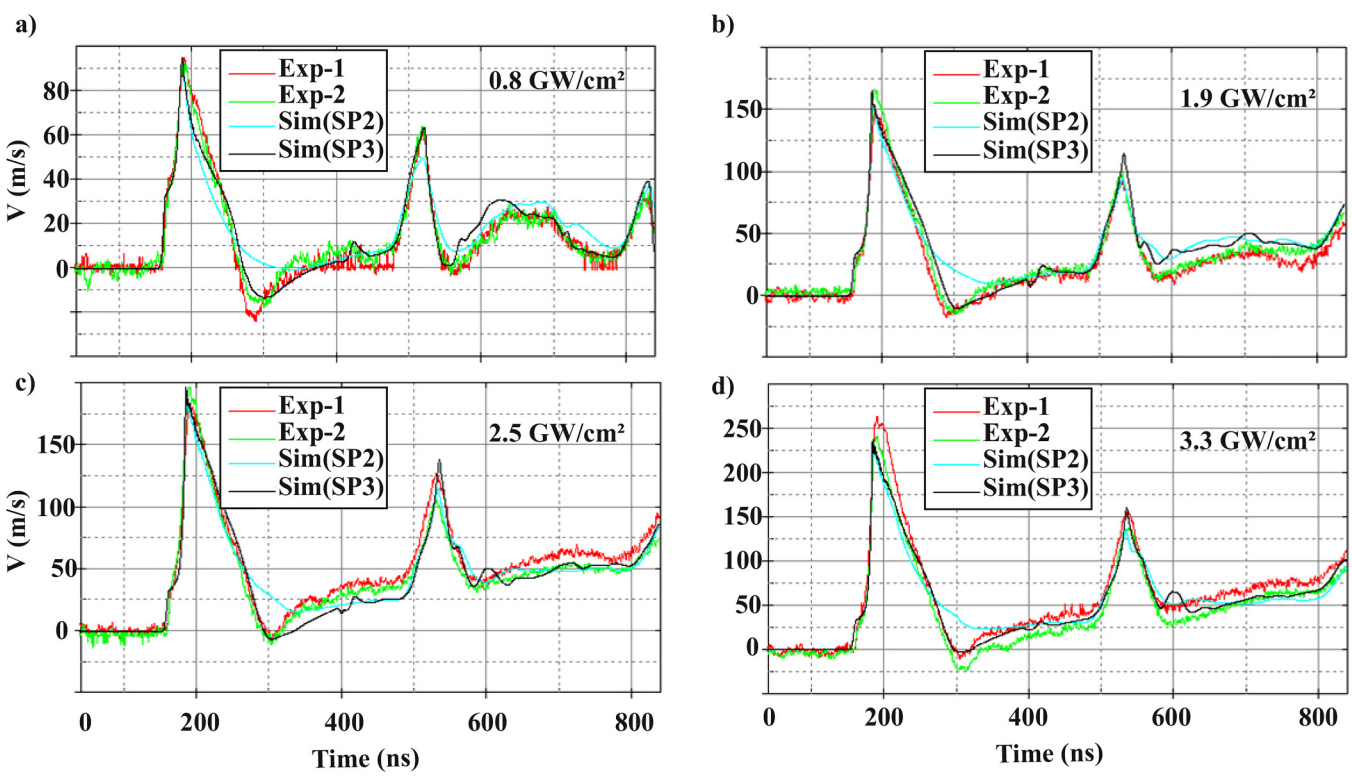

FIG. 13. Comparison of BFV profiles for pure-AL between experimental measurements under 0.7, 1.8, 2.46, and 3.3 GW/cm^2 and the numerical results under 0.8, 1.9, 2.5, and 3.3 GW/cm^2 power density in (a), (b), (c), and (d) accordingly using a 3 mm focal spot.

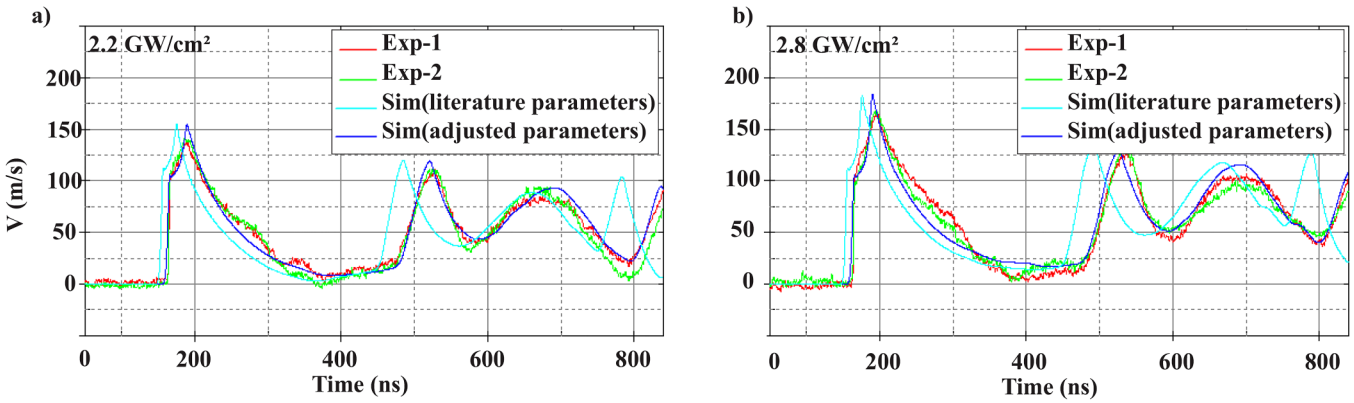

FIG. 14. Comparison of BFV for AA2024-T3 between experimental laser shock under 2.5 and 3 GW/cm^2 power density and the numerical results under 2.2 and 2.8 GW/cm^2 power density in (a) and (b) accordingly using the smoothed spatial distribution SP2 for the 4 mm focal spot [Fig. 8(b)].

should be decreased until the numerical first shock breaks out at the same time the experimental does, which we found equal to 4880 m/s as shown by the BFV profile (blue curve) in Fig. 14 under two different laser intensities [**Sim(adjusted parameters)**]. The used spatial profile SP2 [Fig. 8(b)] was enough to model the dynamical behavior of the 970 μm of AA2024-T3 since edge effects are negligible as shown by the experimental BFV profiles (**Exp-1** and **Exp-2**) in Fig. 14.

VI. DISCUSSION

The selection of proper modeling of loading conditions as the spatial and temporal distribution of power density is of crucial importance to obtain the accurate dynamical response of metallic structures under high strain rate laser shock. In this study, we used the LS-DYNA explicit solver to simulate our laser shock propagation through aluminum alloys. As a material model in LS-DYNA, we used the Johnson-Cook (J-C) material model (MAT_015) coupled with Grüneisen EOS (EOS_GRUNEISEN) (Tables I and II) to describe material behavior under high strain rate deformation produced by laser shock.

To analyze separately the influence of loading conditions on the BFV profile during laser shock, we started with the well-known and studied pure-AL material in the literature under the high strain rate regime. We simulate the BFV profile using the smooth and the sharp spatial laser distribution [SP2 and SP3 in Fig. 8(a)]. The simulated BFV profile using the sharp SP3 profile stimulates the edge effects (negative velocity after the first shock). For the temporal pressure, we used the scale laws of Scius-Bertrand *et al.*[15] while taking into account the rarefaction phenomenon defined in Sec. IV A 1 for the 3 mm focal spot (PT2 in Fig. 5).

In order to analyze the source of these edge effects, we used the X-T code provided by DYNAS+, for pure-AL under 3.3 GW/cm^2 in Fig. 10, where the decrease in the velocity after the first shock on the back face is related to a tensile stress values σ_{yy} on the back face. Afterward, we analyzed the relation between these edge effects and the ratio between the sample thickness and the laser focal spot (R), we found that first edge effect vanishes or the solution will converge toward the 1D solution in Fig. 7 when R$\leq$0.15 as we summarized in Table III. Therefore, according to the existence of these edge effects, the spatial pressure profile slope will be selected from the extreme smooth profile [SP2 in Figs. 8(a) and 8(b)] until the sharp profile [SP3 in Figs. 8(a) and 8(b)].

By comparing the BFV profile simulated using the 1D-approach (Fig. 7) and the one using LS-DYNA for power density of 0.7 GW/cm^2, we can see that the third peak [point G in Fig. 12(b)] is related to 2D phenomena. Figure 12(a) elucidates the origin of this peak which appears to be related to a compression wave that reaches the back face, σ_{yy} contours can also show the origin of this peak which is the convergence of 2D waves and reflected 2D waves [point E and F in Fig. 12(c)] toward the back face. Moreover, we demonstrated that these compressive 2D effects depend on the applied pressure with respect to the Hugoniot elastic limit. They vanish for $P_{max}/P_{HEL} \geq 13$ as summarized in Table III. We validate these numerical sensitivity studies with experimental velocity measurement for 1 mm pure-AL thickness using four different laser intensities as shown in Fig. 13.

TABLE III. Origin of pure-AL and AA2024-T3 BFV profiles peaks according to their timing position including Edge and compressive 2D effects.

Notations	Definition
(a)	Shoulder separating the fast elastic wave from the slower plastic wave[21,59]
(b)	1st shock breaking out
(c)	2nd shock breaking out that corresponds to the back and forth of the first one
(d)	3rd shock breaking out that corresponds to the back and forth of the second one
(e)	Signature of the edge effect on the BFV: tensile stress concentration of σ_{yy} related to the focal spot size and the sample thickness, where it vanishes when: $h/\Phi \leq 0.15$
(g)	2D shock breaking out that vanishes when $P_{max}/P_{HEL} \geq 13$

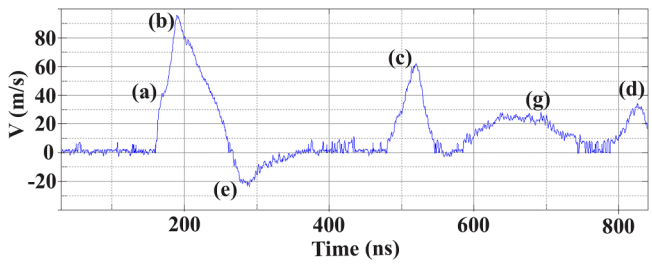

FIG. 15. BFV measurements using VISAR for pure-aluminum-1 mm thickness using a 3 mm focal spot under a 0.7 GW/cm^2 power density.

After validating the numerical inputs using the pure-AL, we adjusted the literature material model parameters of AA2024-T3 to reproduce the experimental measured BFV profiles as shown in Fig. 14. The adjusted model of AA2024-T3 is used to also verify the sensitivity study of edge and compressive 2D effects that have been done on pure-AL as summarized in Table III.

Mastering back face velocity measurement during laser shock has allowed quantifying different phenomena (edge effects, 2D effects, etc.). In order to complete the detailed description of the BFV profile that we started to do with the 1D results as in Table III, we use the BFV profile that of pure-AL (1 mm thickness) under a 0.7 GW/cm^2 laser intensity as depicted in Fig. 15 where edge and compressive 2D effects exist where points (a, b, c, and d) have been identified in Table III.

After validating numerical models of pure-AL and AA2024-T3, we calculated the strain rate during laser shock on these two targets in the function of different laser intensities as shown in Fig. 16 in Appendix C, where the strain rate of deformation can reach $10^7\,s^{-1}$ in pure-AL (1 mm thickness) and AA2024-T3 (970 μm) under 2 and 2.5 GW/cm^2 accordingly.

VII. CONCLUSION

In this study, we demonstrated that wave propagation simulations using LS-DYNA reproduce all experimental phenomena that exist during laser shock propagation. Results demonstrated that loading conditions should be investigated before adjusting the material model parameters. What is more, we investigated the multi edges effects and their signature on the BFV profile for pure-AL and AA2024-T3 during laser shock and we provided conditions where these effects can be stimulated or avoided. We aspire that these numerical and experimental tools could provide a high accuracy material characterization under a high strain rate deformation of aluminum alloys.

ACKNOWLEDGMENTS

This work was supported by Délégation Générale pour l'Armement (DGA) Rapid during the Vanesses project. We acknowledge the financial support from the state budget by the Slovenian Research Agency (Programme No. P2-0270), Erasmus+ KA1 staff mobility programme and bilateral Project BI-FR/20-21-010 between Republic of France and Republic of Slovenia.

AUTHOR DECLARATIONS

Conflict of Interest

The authors have no conflicts to disclose.

DATA AVAILABILITY

The data that support the findings of this study are available from the corresponding author upon reasonable request.

APPENDIX A: DEVELOPMENTS FOR ELASTIC UNIAXIAL STRESS WAVE PROPAGATION

The mechanical problem is governed by the following set of equations:

$$\begin{cases} \mathbf{div}(\boldsymbol{\sigma}) = \rho \frac{\partial^2 \boldsymbol{u}}{\partial t^2} & \text{Balanceoflinearmomentum} \\ \boldsymbol{\sigma} = \mathbb{C} : \boldsymbol{\varepsilon}_e = \mathbb{C} : (\boldsymbol{\varepsilon} - \boldsymbol{\varepsilon}_p) & \text{Elastic law} \\ \boldsymbol{\varepsilon}(\boldsymbol{u}) = \frac{1}{2}(\nabla \boldsymbol{u} + \nabla^{\mathrm{T}} \boldsymbol{u}) & \text{Strain} - \text{displacementrelation} \end{cases}, \tag{A1}$$

where $\boldsymbol{\sigma}$ refers to the stress tensor, $\boldsymbol{\varepsilon}$ refers to the total strain tensor, $\boldsymbol{\varepsilon}_p$ refers to the plastic strain tensor, $\boldsymbol{\varepsilon}_e$ refers to the elastic strain tensor, and $\boldsymbol{u}$ refers to the displacement field. Furthermore, ρ is the density and $\mathbb{C}$ is the stiffness tensor. The elastic behavior of the material is assumed to be isotropic, so that the matrix $\mathbb{C}$ can be reduced to

$$\mathbb{C} = 3\kappa \mathbb{J} + 2\mu \mathbb{K}, \tag{A2}$$

where κ and μ are, respectively, the bulk and shear moduli, and $\mathbb{J}$ and $\mathbb{K}$ are fourth-order tensors defined as

$$\mathbb{J} = \frac{1}{3} \boldsymbol{I} \otimes \boldsymbol{I} \quad \text{and} \quad \mathbb{K} = \mathbb{I} - \mathbb{J}, \tag{A3}$$

with $\boldsymbol{I}$ being the second-order identity tensor and $\mathbb{I}$ being the fourth-order identity tensor. The notation $\otimes$ refers to the so-called outer product. If $\mathbb{M} = \boldsymbol{a} \otimes \boldsymbol{b}$ ($\boldsymbol{a}$ and $\boldsymbol{b}$ being second-order tensors), then

$$\mathbb{M}_{ijkl} = a_{ij} b_{kl}. \tag{A4}$$

Furthermore, the double dot product in Eq. (A1) can be defined as

$$(\mathbb{M} : \boldsymbol{a})_{ij} = \sum_{k,l} M_{ijkl} a_{kl}. \tag{A5}$$

Supposing a uniaxial strain state in the x_1 direction, the mechanical fields have the following forms:

$$\begin{cases} \boldsymbol{u} = u_1(x_1)\boldsymbol{e}_1, \quad \boldsymbol{\varepsilon} = \varepsilon_{11}(x_1, t)\boldsymbol{e}_1 \otimes \boldsymbol{e}_1 \\ \boldsymbol{\sigma} = \sigma_{11}(x_1, t)\boldsymbol{e}_1 \otimes \boldsymbol{e}_1 + \sigma_{22}(x_1, t)(\boldsymbol{e}_2 \otimes \boldsymbol{e}_2 + \boldsymbol{e}_3 \otimes \boldsymbol{e}_3) \end{cases}, \tag{A6}$$

where $\varepsilon_{11} = \partial u_1 / \partial x_1$.

Using the previous hypotheses, the stress wave propagation equations are derived for this simplified 1D problem. The propagation will be assumed to be purely elastic so that we have $\dot{\boldsymbol{\varepsilon}}_p = 0$.

The mechanical fields only depend on one spatial coordinate, x_1. As a consequence, the first two equations of system (A1) lead to the partial derivative system,

$$\begin{cases} \frac{\partial \sigma_{11}}{\partial x_1}(x_1, t) = \rho \frac{\partial v_1}{\partial t}(x_1, t) \\ \frac{\partial \sigma_{11}}{\partial t}(x_1, t) = \left(\kappa + \frac{4}{3}\mu\right) \frac{\partial \varepsilon_{11}}{\partial t}(x_1, t) = \left(\kappa + \frac{4}{3}\mu\right) \frac{\partial v_1}{\partial x_1}(x_1, t) \end{cases}, \tag{A7}$$

since $\partial \varepsilon_{11}/\partial t = \partial^2 u/\partial t \partial x_1 = \partial v_1/\partial x_1$. From system (A7), it is straightforward to deduce the stress wave equation (1).

APPENDIX B: RADIAL RETURN ALGORITHM

We present here the pseudo-code algorithm used to compute the radial return allowing the problem to verify the Eq. (8) during an elasto-plastic propagation.

Remark 1 During the elastic trial state, the total strain is computed using $\frac{\partial \varepsilon_{11}}{\partial t} = \frac{\partial v_1}{\partial x_1}$. This equation being independent of plasticity, the computed value for the total strain is also valid in the radial return part of the algorithm, where it is needed to correct the stress.

Remark 2 For the computation of the new plastic flow stress, we introduce the function R^* line 11 of Algorithm 16 such that $R(\bar{\boldsymbol{\varepsilon}}_p^{k+1}, \dot{\bar{\boldsymbol{\varepsilon}}}_p^{k+1}) = R^*(p^k, \Delta p)$. The Johnson-Cook model depends on the quantities $\bar{\boldsymbol{\varepsilon}}_p$ and $\dot{\bar{\boldsymbol{\varepsilon}}}_p$, which can be both expressed as functions of Δp by the definition of the accumulated plastic strain rate $\dot{p}$. More precisely, $\bar{\boldsymbol{\varepsilon}}_p^{k+1} = \bar{\boldsymbol{\varepsilon}}_p^k + \Delta \bar{\boldsymbol{\varepsilon}}_p = \bar{\boldsymbol{\varepsilon}}_p^k + \Delta p$. We can, thus, define a function R^*, equivalent to R, depending explicitly on Δp. In line 11 of the algorithm, the quantity p^{k+1} is used as argument for the function R^* so that the equation is solved for the new value of the yield flow stress at each iteration, not just the one when plasticity was detected.

Algorithm 1 Simulation of the elasto plastic uniaxial stress wave propagation

1: Input variables : σ_{11}^k, σ_{22}^k, ε_{11}^k, $\varepsilon_{p,11}^k$, p^k, R^k.
2: Compute $\sigma_{11}^{\text{trial}}$, v_1^{k+1} with the numerical method assuming an elastic evolution.
3: Compute the corresponding ε_{11}^{k+1} and $\sigma_{22}^{\text{trial}}$ values.
4: Elastic trial : $\varepsilon_{p,11}^{k+1} = \varepsilon_{p,11}^k$ and $p^{k+1} = p^k$
5: **if** $J_2(\sigma^{\text{trial}}) - R^k \leq 0$ **then**
6: $\quad \sigma^{k+1} = \sigma^{\text{trial}}$
7: $\quad$ **End**
8: **else**
9: $\quad$ Initialize Δp, and $\sigma^{k+1} = \sigma^{\text{trial}}$
10: $\quad$ while $\Delta p > \epsilon$ **do** $\quad \triangleright \epsilon$ is a given tolerance
11: $\quad\quad$ Find Δp such that $J_2(\sigma^{k+1}) - 3\mu\Delta p - R^*(p^{k+1}, \Delta p) = 0$.
12: $\quad\quad$ Compute $\Delta \varepsilon_p = \frac{3}{2} \frac{S^{k+1}}{J_2(\sigma^{k+1})} \Delta p$
13: $\quad\quad$ Compute ε_p^{k+1} and p^{k+1} using $\Delta \varepsilon_p$ and Δp.
14: $\quad\quad$ Compute $R^{k+1} = R(\bar{\varepsilon}_p^{k+1}, \dot{\bar{\varepsilon}}_p^{k+1})$
15: $\quad\quad$ Compute the new stress state :
$\quad\quad$ $\sigma^{k+1} = \kappa \text{Tr}(\varepsilon^{k+1}) I + S^{k+1} - 2\mu\Delta\varepsilon_p$
16: $\quad$ **End**

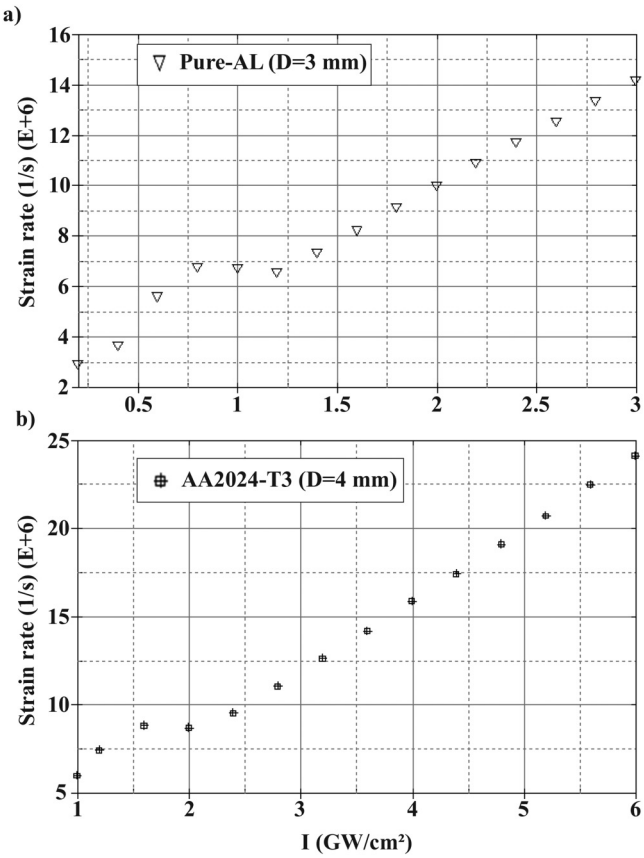

FIG. 16. Strain rate in pure-AL (1 mm thickness) and AA2024-T3 (970 μm thickness) for different applied power densities accordingly in a and b.

APPENDIX C: STRAIN RATE IN PURE-AL AND AA2024-T3

Using the validated material model and loading conditions on the pure-AL and on the AA2024-T3, we calculate the strain rate of deformation for different power densities [I (GW/cm^2)] as shown in Fig. 16.

APPENDIX D: ANALYTICAL FIT OF THE SPATIAL POWER DENSITY

We provide the analytical fittings of the spatial power density for the smooth and sharp filtered profiles in Table IV, where $\alpha = 2.76(\text{mm})/\text{FWHM}(\text{mm})$, and FWHM is the Full Width at Half Maximum of the spatial profile.

TABLE IV. Analytical fit of the normalized filtered spatial power density.

SP	Spatial position	Normalized power density
SP2	$0 \le x \le 0.14 \times \mathrm{FWHM}$	$I_r(x) = 1$
	$0.14 \times \mathrm{FWHM} \le x \le 0.544 \times \mathrm{FWHM}$	$I_r(x) = 0.279(\alpha x)^4 - 1.137(\alpha x)^3 + 1.13(\alpha x)^2 - 0.487(\alpha x) + 1.08$
	$0.544 \times \mathrm{FWHM} \le x \le 0.993 \times \mathrm{FWHM}$	$I_r(x) = -0.198(\alpha x)^4 + 1.46(\alpha x)^3 - 3.428(\alpha x)^2 + 2.088(\alpha x) + 1.126$
	$0.993 \times \mathrm{FWHM} \le x \le 2 \times \mathrm{FWHM}$	$I_r(x) = 0$
SP3	$0 \le x \le 0.267 \times \mathrm{FWHM}$	$I_r(x) = 1$
	$0.267 \times \mathrm{FWHM} \le x \le 0.4566 \times \mathrm{FWHM}$	$I_r(x) = -10.023(\alpha x)^4 + 36.327(\alpha x)^3 - 49.374(\alpha x)^2 + 29.774(\alpha x) - 5.714$
	$0.457 \times \mathrm{FWHM} \le x \le 0.522 \times \mathrm{FWHM}$	$I_r(x) = 88.694(\alpha x)^3 - 359.09(\alpha x)^2 + 480.56(\alpha x) - 212.01$
	$0.522 \times \mathrm{FWHM} \le x \le 0.7826 \times \mathrm{FWHM}$	$I_r(x) = -2.657(\alpha x)^5 + 27.642(\alpha x)^4 - 114.57(\alpha x)^3 + 236.47(\alpha x)^2 - 243.08(\alpha x) + 99.588$
	$0.783 \times \mathrm{FWHM} \le x \le 2 \times \mathrm{FWHM}$	$I_r(x) = 0$

REFERENCES

[1]K. Langer, T. J. Spradlin, and M. E. Fitzpatrick, "Finite element analysis of laser peening of thin aluminum structures," Metals **10**, 93 (2020).

[2]B. Wu and Y. C. Shin, "A self-closed thermal model for laser shock peening under the water confinement regime configuration and comparisons to experiments," J. Appl. Phys. **97**, 113517 (2005).

[3]Y. Liao, C. Ye, B.-J. Kim, S. Suslov, E. A. Stach, and G. J. Cheng, "Nucleation of highly dense nanoscale precipitates based on warm laser shock peening," J. Appl. Phys. **108**, 063518 (2010).

[4]C. Ye, S. Suslov, D. Lin, Y. Liao, X. Fei, and G. J. Cheng, "Microstructure and mechanical properties of copper subjected to cryogenic laser shock peening," J. Appl. Phys. **110**, 083504 (2011).

[5]P. Peyre, L. Berthe, X. Scherpereel, and R. Fabbro, "Laser-shock processing of aluminium-coated 55C1 steel in water-confinement regime, characterization and application to high-cycle fatigue behaviour," J. Mater. Sci. **33**, 1421–1429 (1998).

[6]P. Peyre, X. Scherpereel, L. Berthe, C. Carboni, R. Fabbro, G. Béranger, and C. Lemaitre, "Surface modifications induced in 316L steel by laser peening and shot-peening. Influence on pitting corrosion resistance," Mater. Sci. Eng., A **280**, 294–302 (2000).

[7]U. Trdan and J. Grum, "Evaluation of corrosion resistance of aa6082-t651 aluminium alloy after laser shock peening by means of cyclic polarisation and els methods," Corros. Sci. **59**, 324–333 (2012).

[8]U. Trdan and J. Grum, "SEM/EDS characterization of laser shock peening effect on localized corrosion of al alloy in a near natural chloride environment," Corros. Sci. **82**, 328–338 (2014).

[9]U. Trdan, T. Sano, D. Klobčar, Y. Sano, J. Grum, and R. Šturm, "Improvement of corrosion resistance of aa2024-t3 using femtosecond laser peening without protective and confining medium," Corros. Sci. **143**, 46–55 (2018).

[10]R. Ecault, F. Touchard, L. Berthe, and M. Boustie, "Laser shock adhesion test numerical optimization for composite bonding assessment," Compos. Struct. **247**, 112441 (2020).

[11]L. Berthe, M. Arrigoni, M. Boustie, J. P. Cuq-Lelandais, C. Broussillou, G. Fabre, M. Jeandin, V. Guipont, and M. Nivard, "State-of-the-art laser adhesion test (LASAT)," Nondestr. Test. Eval. **26**, 303–317 (2011).

[12]S. Sadeh, G. H. Gleason, M. I. Hatamleh, S. F. Sunny, H. Yu, A. S. Malik, and D. Qian, "Simulation and experimental comparison of laser impact welding with a plasma pressure model," Metals **9**, 1196 (2019).

[13]S. Ünaldi, K. Papadopoulos, A. Rondepierre, Y. Rouchausse, A. Karanika, F. Deliane, K. Tserpes, G. Floros, E. Richaud, and L. Berthe, "Towards selective laser paint stripping using shock waves produced by laser-plasma interaction for aeronautical applications on AA 2024 based substrates," Opt. Laser Technol. **141**, 107095 (2021).

[14]K. Tserpes, K. Papadopoulos, S. Unaldi, and L. Berthe, "Development of a numerical model to simulate laser-shock paint stripping on aluminum substrates," Aerospace **8**, 233 (2021).

[15]M. Scius-Bertrand, L. Videau, A. Rondepierre, E. Lescoute, Y. Rouchausse, J. Kaufman, D. Rostohar, J. Brajer, and L. Berthe, "Laser induced plasma characterization in direct and water confined regimes: New advances in experimental studies and numerical modelling," J. Phys. D: Appl. Phys. **54**, 055204 (2020).

[16]P. Peyre and R. Fabbro, "Laser shock processing: A review of the physics and applications," Opt. Quantum Electron. **27**, 1213–1229 (1995); available at https://app.dimensions.ai/details/publication/pub.1085146353

[17]N. C. Anderholm, "Laser-generated stress waves," Appl. Phys. Lett. **16**, 113–115 (1970).

[18]L. Berthe, R. Fabbro, P. Peyre, L. Tollier, and E. Bartnicki, "Shock waves from a water-confined laser-generated plasma," J. Appl. Phys. **82**, 2826–2832 (1997).

[19]C. Le Bras, A. Rondepierre, R. Seddik, M. Scius-Bertrand, Y. Rouchausse, L. Videau, B. Fayolle, M. Gervais, L. Morin, S. Valadon, R. Ecault, D. Furfari, and L. Berthe, "Laser shock peening: Toward the tse of pliable polid polymers for confinement," Metals **9**, 793 (2019).

[20]C. Le Bras, A. Rondepierre, M. Ayad, Y. Rouchausse, M. Gervais, S. Valadon, and L. Berthe, "Novel confinement possibility for laser shock: Use of flexible polymer confinement at 1064 nm wavelength," Metals **11**, 1467 (2021).

[21]P. Ballard, "Contraintes résiduelles induites par impact rapide. Application au choc laser," Ph.D. thesis (Ecole Polytechnique, 1991).

[22]E. Troiani and N. Zavatta, "The effect of laser peening without coating on the fatigue of a 6082-t6 aluminum alloy with a curved notch," Metals **9**, 728 (2019).

[23]R. Ecault, F. Touchard, M. Boustie, L. Berthe, and N. Dominguez, "Numerical modeling of laser-induced shock experiments for the development of the adhesion test for bonded composite materials," Compos. Struct. **152**, 382–394 (2016).

[24]R. Ecault, L. Berthe, F. Touchard, M. Boustie, E. Lescoute, A. Sollier, and H. Voillaume, "Experimental and numerical investigations of shock and shear wave propagation induced by femtosecond laser irradiation in epoxy resins," J. Phys. D: Appl. Phys. **48**, 095501 (2015).

[25]Y. Hu, Z. Yao, and J. Hu, "3-D FEM simulation of laser shock processing," Surf. Coat. Technol. **201**, 1426–1435 (2006).

[26]X. Wu, Z. Duan, H. Song, Y. Wei, X. Wang, and C. Huang, "Shock pressure induced by glass-confined laser shock peening: Experiments, modeling and simulation," J. Appl. Phys. **110**, 053112 (2011).

[27]M. Boustie, J. P. Cuq-Lelandais, C. Bolis, L. Berthe, S. Barradas, M. Arrigoni, T. De Resseguier, and M. Jeandin, "Study of damage phenomena induced by edge effects into materials under laser driven shocks," J. Phys. D: Appl. Phys. **40**, 7103–7108 (2007).

[28]R. Fabbro, J. Fournier, P. Ballard, D. Devaux, and J. Virmont, "Physical study of laser-produced plasma in confined geometry," J. Appl. Phys. **68**, 775–784 (1990).

[29]A. Rondepierre, S. Ünaldi, Y. Rouchausse, L. Videau, R. Fabbro, O. Casagrande, C. Simon-Boisson, H. Besaucèle, O. Castelnau, and L. Berthe, "Beam size dependency of a laser-induced plasma in confined regime: Shortening of the plasma release. Influence on pressure and thermal loading," Opt. Laser Technol. **135**, 106689 (2021).

[30]S. Bardy, B. Aubert, T. Bergara, L. Berthe, P. Combis, D. Hébert, E. Lescoute, Y. Rouchausse, and L. Videau, "Development of a numerical code for laser-induced shock waves applications," Opt. Laser Technol. **124**, 105983 (2020).
[31]L. Wang, *Foundations of Stress Waves* (Elsevier, 2005).
[32]T. Heuzé, "Lax–Wendroff and TVD finite volume methods for unidimensional thermomechanical numerical simulations of impacts on elastic–plastic solids," J. Comput. Phys. **346**, 369–388 (2017).
[33]G. R. Johnson and W. H. Cook, "A constitutive model and data for metals subjected to large strains, high strain rates and high temperatures" (International Ballistics Society, Hague, 1983), pp. 541–547.
[34]M. Sticchi, P. Staron, Y. Sano, M. Meixer, M. Klaus, J. Rebelo–Kornmeier, N. Huber, and N. Kashaev, "A parametric study of laser spot size and coverage on the laser shock peening induced residual stress in thin aluminium samples," J. Eng. **2015**, 97–105 (2015).
[35]T. J. Spradlin, R. V. Grandhi, and K. Langer, "Experimental validation of simulated fatigue life estimates in laser-peened aluminum," Int. J. Struct. Integr. **2**, 74–86 (2011).
[36]P. Peyre, L. Berthe, V. Vignal, I. Popa, and T. Baudin, "Analysis of laser shock waves and resulting surface deformations in an Al–Cu–Li aluminum alloy," J. Phys. D: Appl. Phys. **45**, 335304 (2012).
[37]M. Bonnet and A. Frangi, *Analyse des Solides Déformables par la Méthode des Éléments Finis*, les Éditions de l'École Polytechnique ed. (Ellipses, 2007).
[38]L. Ming and O. Pantalé, "An efficient and robust VUMAT implementation of elastoplastic constitutive laws in Abaqus/Explicit finite element code," Mech. Ind. **19**, 308 (2018).
[39]T. Heuzé, "Lax-Wendroff schemes for elastic-plastic solids," J. Comput. Phys. **396**, 89–105 (2019).
[40]R. J. Leveque, *Finite Volume Methods for Hyperbolic Problems* (Cambridge University Press, 2002), p. 580.
[41]B. O'Toole, M. Trabia, R. Hixson, S. K. Roy, M. Pena, S. Becker, E. Daykin, E. MacHorro, R. Jennings, and M. Matthes, "Modeling plastic deformation of steel plates in hypervelocity impact experiments," Procedia Eng. **103**, 458–465 (2015).
[42]T. Børvik, M. Langseth, O. Hopperstad, and K. Malo, "Ballistic penetration of steel plates," Int. J. Impact Eng. **22**, 855–886 (1999).
[43]D. J. Bammann, M. L. Chiesa, G. C. Johnson, T. Tatsumi, T. Kambe, and E. Watanabe, *Modeling Large Deformation and Failure in Manufacturing Processes, International Congress; 19th, Theoretical and Applied Mechanics* (Elsevier, 1997), pp. 359–378.
[44]S. Bhamare, G. Ramakrishnan, S. R. Mannava, K. Langer, V. K. Vasudevan, and D. Qian, "Simulation-based optimization of laser shock peening process for improved bending fatigue life of Ti-6Al-2Sn-4Zr-2Mo alloy," Surf. Coat. Technol. **232**, 464–474 (2013).
[45]M. Meyers, *Dynamic Behavior of Materials*, Wiley-Interscience Publication (Wiley, 1994).
[46]K. Langer, S. Olson, R. Brockman, W. Braisted, T. Spradlin, and M. E. Fitzpatrick, "High strain–rate material model validation for laser peening simulation," J. Eng. **2015**, 150–157 (2015).
[47]P. Peyre, I. Chaieb, and C. Braham, "FEM calculation of residual stresses induced by laser shock processing in stainless steels," Modell. Simul. Mater. Sci. Eng. **15**, 205–221 (2007).
[48]F. Plassard, J. Mespoulet, and P. Hereil, "Hypervelocity impact of aluminium sphere against aluminium plate: Experiment and LS-DYNA correlation," in *8th European LS-DYNA Users Conference* (DYNAlook, Strasbourg, 2011), pp. 1–11.
[49]D. Grady, "The shock wave equation of state," in *Physics of Shock and Impact* (IOP Publishing, 2017), Vol. 2, pp. 2053–2563.
[50]L. Barker and R. Hollenbach, "Laser interferometer for measuring high velocities of any reflecting surface," J. Appl. Phys. **43**, 4669–4675 (1972).
[51]L. M. Barker and K. W. Schuler, "Correction to the velocity–per–fringe relationship for the visar interferometer," J. Appl. Phys. **45**, 3692–3693 (1974).
[52]R. Seddik, A. Rondepierre, S. Prabhakaran, L. Morin, V. Favier, T. Palin-Luc, and L. Berthe, "Identification of constitutive equations at very high strain rates using shock wave produced by laser," Eur. J. Mech. A Solids **92**, 104432 (2022).
[53]Z. Wang, M. Shi, J. Gan, X. Wang, Y. Yang, and X. Ren, "The effects of shot distance and impact sequence on the residual stress field in shot peening finite element model," Metals **11**, 1–19 (2021).
[54]See http://www.matweb.com for "Online materials information resource-matweb" (accessed 23 March 2021).
[55]R. Fabbro, J. Fournier, P. Ballard, D. Devaux, and J. Virmont, "Physical study of laser–produced plasma in confined geometry," J. Appl. Phys. **68**, 775–784 (1990).
[56]S. Bardy, "Contrôle et optimisation du test d'adhérence par choc laser sur assemblages collés," Theses (Ecole Nationale Supérieure d'Arts et Métiers - ENSAM, 2017).
[57]A. N. Pirri, "Theory for momentum transfer to a surface with a high-power laser," Phys. Fluids **16**, 1435–1440 (1973).
[58]T. Sakka, K. Takatani, Y. Ogata, and M. Mabuchi, "Laser ablation at the solid-liquid interface: Transient absorption of continuous spectral emission by ablated aluminium atoms," J. Phys. D: Appl. Phys. **35**, 65–73 (2002).
[59]J. A. Smith, J. M. Lacy, D. Lévesque, J. P. Monchalin, and M. Lord, "Use of the Hugoniot elastic limit in laser shockwave experiments to relate velocity measurements," AIP Conf. Proc. **1706**, 080005 (2016).